Electronic Supplementary Information

Retrieving Subwavelength Cross-section of Dielectric Nanowires with Asymmetric Excitation of Bloch Surface Waves

Xi Tang, Yan Kuai, Zetao Fan, Zhiyu Zhang, and Douguo Zhang*

Advanced Laser Technology Laboratory of Anhui Province, Department of Optics and Optical

Engineering, University of Science and Technology of China, Hefei, Anhui, 230026, China

*E-mail: dgzhang@ustc.edu.cn

This Supporting Information file includes additional details about Manufacturing procedures of

multilayer and nanowires (Fig. S1); Schematics of experimental set-up and characterization of samples

((Figs. S2, S3); Details for dealing images and data ((Fig. S4); Influence of the slightly tilted illumination

in x-y plane (Fig. S5); Detailed derivation of row dipoles model (Part 1 and Part 2); Discussion of optical

metrology measurement (Figs S6-S9).

Manufacturing procedures of multilayer and nanowires

The initial dielectric multilayers were fabricated via plasma-enhanced chemical vapor deposition (PECVD; System 100, Oxford Instruments) of SiO_2 and Si_3N_4 on a standard microscope cover glass (thickness: 0.17 mm) at a vacuum of <0.1 mtorr and temperature of 300°C. The cover glass was pre-cleaned, first using a piranha solution and then using nanopure deionized water, and was subsequently dried using a N_2 stream. The structure was composed of four pairs of the SiO_2 and Si_3N_4 layers. The thickness of SiO_2 layer and Si_3N_4 layer was approximately 135 nm and 128 nm, respectively. An additional Si_3N_4 layer was deposited on the top surface and was used to fabricate dielectric nanowires of various widths. A negative photoresist layer composed of hydrogen silsesquioxane (HSQ) polymer was spin-coated onto the dielectric multilayer structure. Then, electron beam lithography (6300FS, JEOL. Japan) and reactive ion etching (RIE; PlasmaPro NGP 80, Oxford Instruments, UK) were used to fabricate the dielectric nanowires on the dielectric multilayer structure. The Heights of all nanowires were characterized using AFM and the widths were characterized via SEM.
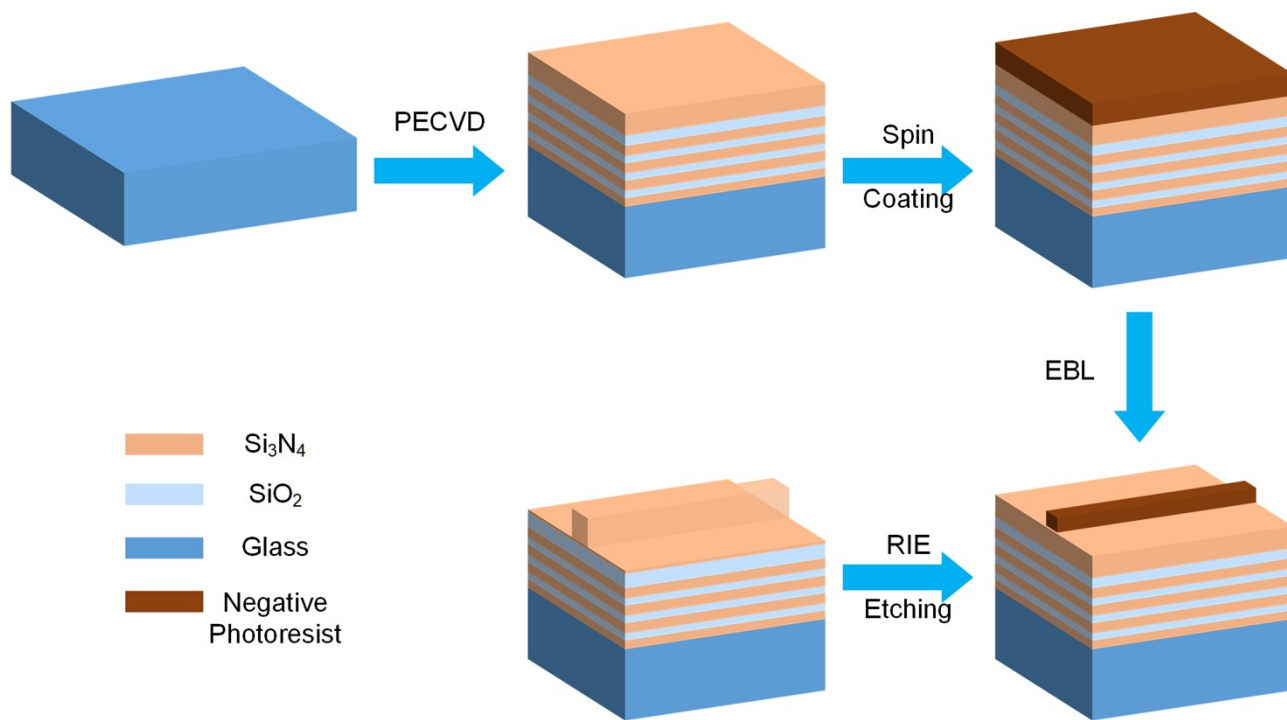

Figure S1. Procedures for fabrication of a sample that contains a single dielectric nanowire on a dielectric multilayer structure.

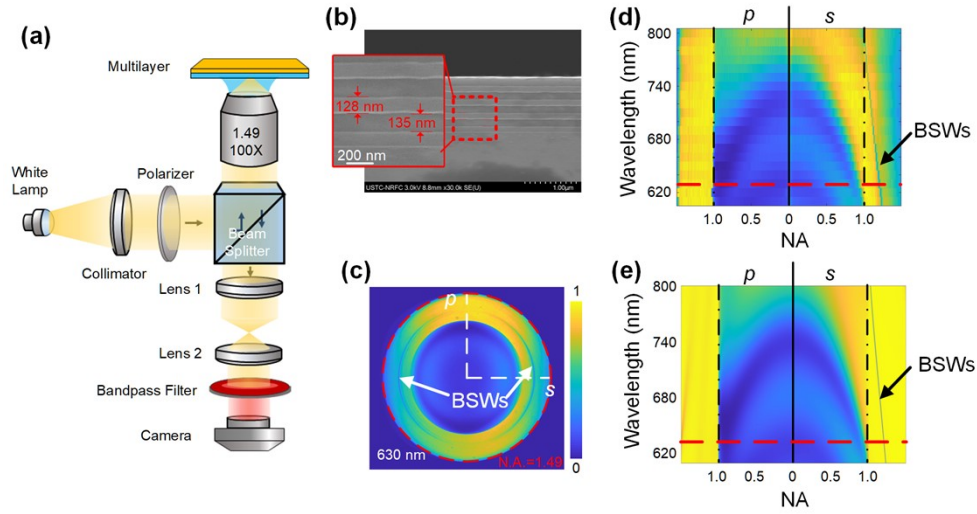**Schematics of experimental set-up and characterization of samples**

Figure S2. Characterization of the dielectric multilayer structure. (a) Schematic of the experimental set up used for reflection back focal plane (BFP) imaging. (b) Scanning electron microscope (SEM) image of the cross-section of multilayer. (c) Reflected BFP image of multilayer at a wavelength of 630 nm. The pair of arcs represents the signature of *s*-polarized BSWs sustained on multilayer. (d) Numerical aperture and wavelength-dependent reflectivity of multilayer as mapped from the BFP images at various wavelengths. (e) Calculated reflectivity characteristics of multilayer. The red dashed lines in (d) and (e) represent the wavelength of the He-Ne laser used in the experiments.

All optical experiments were performed on an in-house-built leaky radiation microscope, as illustrated in Figs. S2 and S3. An oil-immersed objective lens (100×, NA of 1.49; Olympus, Japan) was used for optical imaging. By tuning the distance between the tube lens and the detector, both front focal plane (FFP) and BFP images of the objective can be captured. The detectors used were scientific complementary metal-oxide-semiconductor (sCMOS) detectors (Neo-sCMOS, Andor, UK) for BFP imaging and a charge-coupled device (CCD) camera (Retiga 6000, QImaging, Canada) for FFP imaging. The schematics of reflective leaky radiation microscopy used for characterizing multilayer is shown in Fig. S2a. A white lamp was used as the light source, and the white light beam was expanded and collimated to fill the rear aperture of the objective (100×, NA = 1.49); it was then focused onto multilayer. A polarizer was used to generate linearly polarized light. The reflected white light beam was collected via the same objective, the BFP of which was imaged onto a camera using Lens 1 and Lens 2. A series of band-pass filters was used to select wavelengths from the white light. For Figs. S2 (d and f), the horizontal axis NA = $n*\sin(\theta)$, where n is 1.515 and θ is the incident angle. The left side of black line is for *p*-polarization, and the right side is for *s*-polarization. Compared the calculated and experimental results, the parameters be acquired. Because the excitation angle of BSWs is sensitive to the thickness of top layer, the curve shown in Fig, 1c can be used to determine the top thickness.

Fig. S3a shows another function of this set-up. Firstly, the FFP images were obtained under illumination by a white light source and were used to confirm the position and orientation of the nanowire. A second laser beam (632.8 nm He-Ne laser, model HNL210L; Thorlabs, USA) was used to illuminate the nanowire obliquely from the top side with an angle of incidence of approximately 60° (transmission mode). The nanowire was placed on the plane of incidence of the laser beam. The transmitted laser beam, the leaky radiation of the BSWs, and other scattering signals were then imaged using the sCMOS detector for transmitted BFP imaging. A combination of a polarizer and a half-wave plate was used to control the polarization orientation of this part of the laser beam (linear polarization). The half-wave plate was installed on a motorized rotation mount (K10CR1/M, Thorlabs, USA). A combination of a zero-order vortex half-wave retarder (WPV10L-633, Thorlabs, USA) and a polarizer was used to filter the polarization states of the transmitted signals for this part of the laser beam. Two series of transmitted BFP image were captured: one series without any nanowires on multilayer used as the background BFP image, and another series with nanowires used for verification of the asymmetric BSWs.
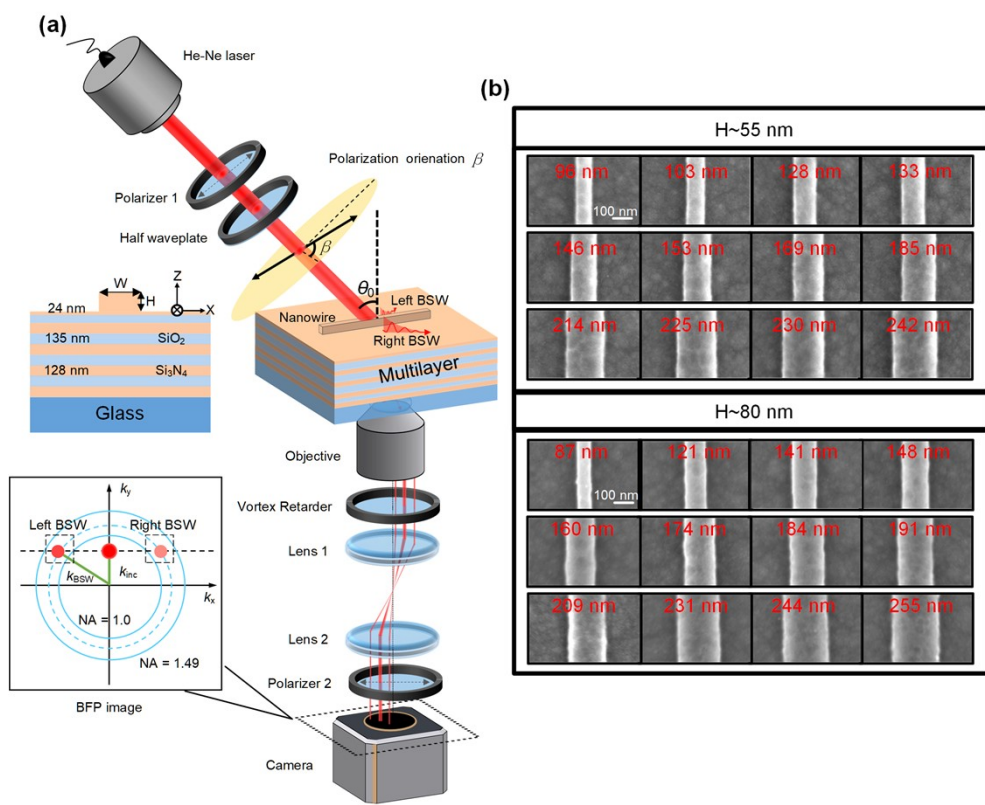

Figure S3. Characterization of nanowires. (a) Schematic of the experimental set up used for transmitted back focal plane (BFP) imaging. (b) Scanning electron microscope (SEM) image of the width of nanowires.

Details for dealing images and data

In this section, we describe the process of data post-processing in three steps.

Step 1: The background BFP image (where there is no nanowire in the field of view) is subtracted from the original BFP image (where the total field contains the direct transmission field and the scattering field), and a BFP image containing only the scattering field from the nanowire is then obtained.

Step 2: The intensity of the left and right BSWs is extracted from the BFP image. The value of this intensity is the sum of the pixel intensities in the areas that contain either the left BSWs or the right BSWs. The extinction ratio ($10\lg(I_{L-R})$) was plotted *vs.* the polarization orientation (β) of the incident light. The process was repeated 40 times to obtain 40 curves.

Step 3: Curves of Ratio vs. β that were plotted for nanowires with various widths and a fixed height were obtained via the same process used in step 2. β_{max} (the polarization orientation for the maximum intensity ratio) was derived from these curves. The relationship between the β_{max} value and the nanowire width is confirmed.
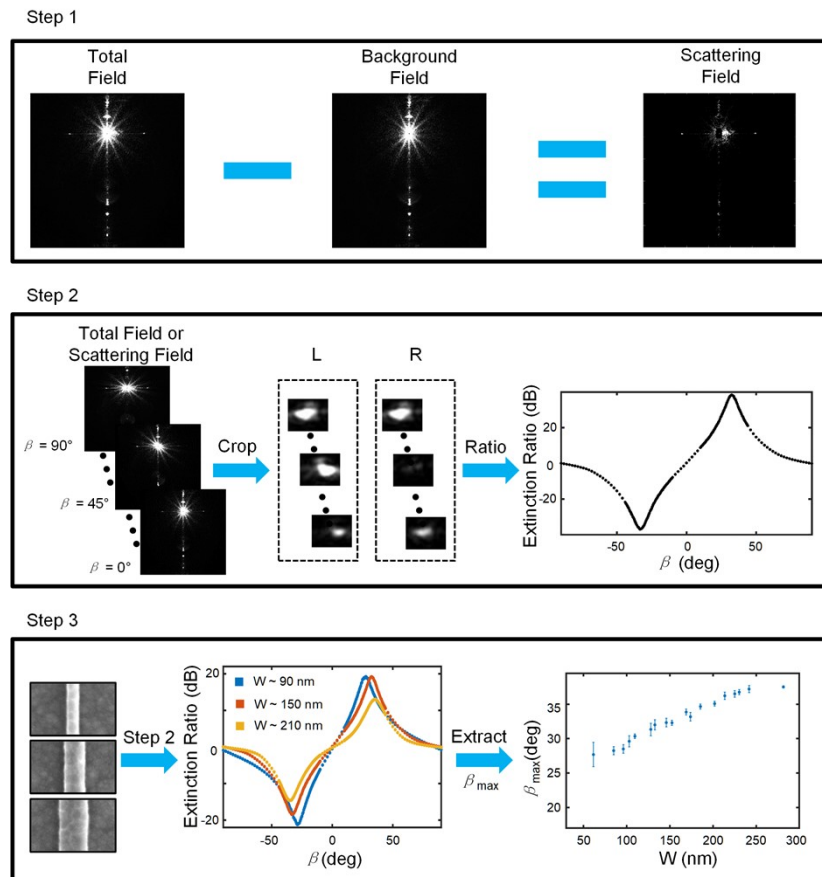
Figure S4. Steps for the data processing.

Influence of the slightly tilted illumination in x-y plane

Here, we discuss the influence of the slightly tilted illumination in x-y plane. In Fig. S5, the inset image presents the schematics of numerical model in x-y plane used for FDTD. Orientation angle γ is defined to characterize the in-plane wavenumber of incident light which may be not strictly parallel to nanowires. The dependence of extinction ratio on incident polarization are shown when orientation angle γ changes from 0° to 5°. The curves would move if orientation angle γ is not zero. The angle interval of polarization is chosen as 0.1°. However, the defined parameter β_{max} obtained from the two curves are the same as each other (Red line: β_{max} = (|-22.1°| + |22.1°|)/2 = 22.1°; Blue line: β_{max} = (|-25.7°| + |18.6°|)/2 = 22.15°). Therefore, step 3 in FIG. S4 take this method to acquire β_{max} and plot curves.
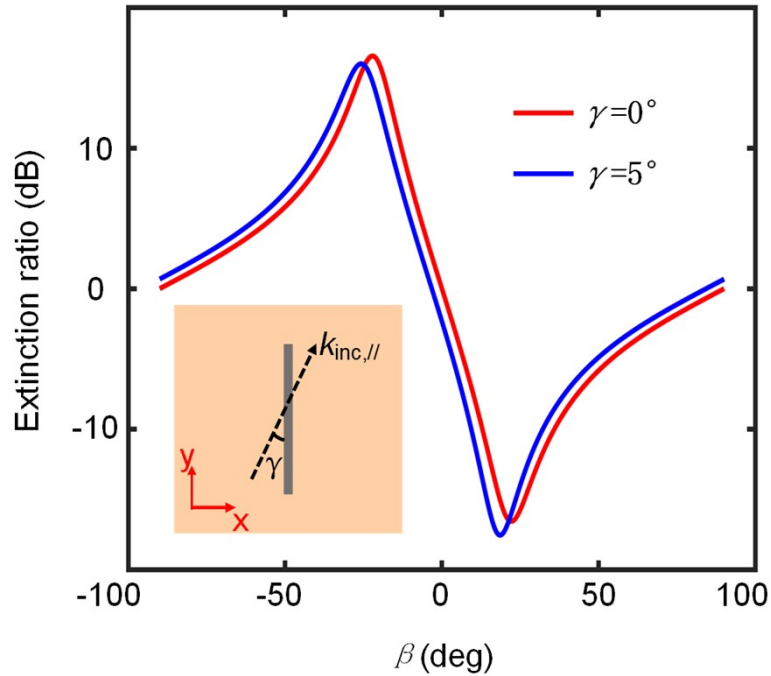

Figure S5. The dependence of Extinction Ratio on incident polarization

Influence of the geometry of the nanowire cross-section

In this section, we discuss that the influence of the geometry of the nanowire cross-section when orientation angle γ is set 0°. For simplicity, we calculate a symmetric hexagonal cross-section nanowire. In Fig. S6, the inset image presents the schematics of numerical model in y-z plane used for FDTD. The height H is fixed at 80 nm. W_{max} is the width of the surrounding rectangle (black dashed rectangle) and W is the width of up and down sides. If the W is 0 nm, the cross-section would be diamond-shape. If the W is 150 nm, the cross-section would be rectangle-shape. The dependence of extinction ratio on incident polarization are shown when the width W changes from 0 nm to 150 nm. From Fig. S6(a), the defined parameter β_{max} obtained from the curves are different from each other. (Black line: βmax = 28.7°; Red line: βmax = 27.4°; Blue line: βmax = 30.9°). Fig. S6(b) shows the βmax varies as W increases. This means the geometry of the nanowire cross-section can influence the optimum polarization for exciting unidirectional BSWs. Additionally, the hexagonal cross-section with equal side has the minimum β_{max}.
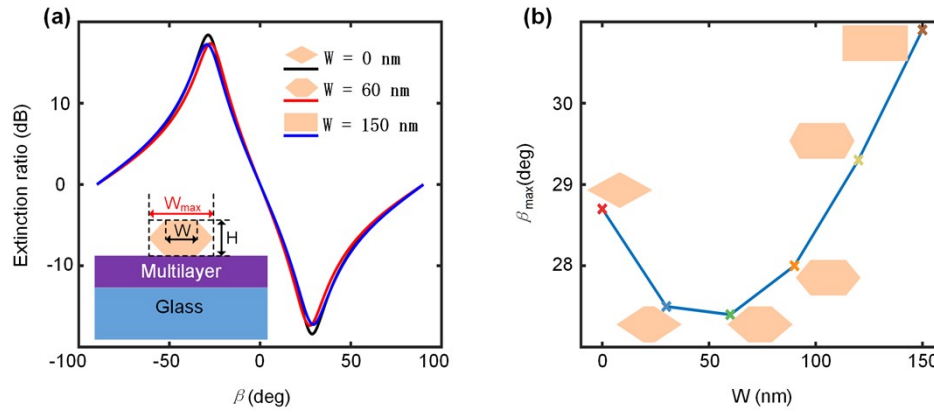

Figure S6. (a)The dependence of Extinction Ratio on incident polarization. (b) Influence of geometric shape of nanowire cross-section.

Table S1. The calculated β_{max} and corresponding width W

W(nm)	0	30	60	90	120	150
β_{max}(°)	28.7	27.5	27.4	28	29.3	30.9

Part 1 Detailed derivation of Equation 1 and 2

In this part, we present the detailed process for the derivation of Eqs. (1-2) in the main text. The vector potential $\mathbf{A(r)}$ of an oscillating electric dipole can be expressed as shown in Eq. (S1) [6-8]:

$$\mathbf{A(r)} = \frac{\mu}{4\pi}[\int_{-\infty}^{+\infty} \mathbf{J(r')}d\mathbf{r'}]\frac{e^{ik_a r}}{r},\qquad(S1)$$

Here, the electric dipole is placed in air. $\mathbf{J}(r')$ is the electric current density and k_a. is the wavenumber of the light in air. Through a process of integration by parts and using the continuity equation of charge, we can acquire the more familiar form shown:

$$\mathbf{A(r)} = -\frac{i\omega\mu}{4\pi}\mathbf{p}\frac{e^{ik_a r}}{r},\qquad(S2)$$

where is the electric dipole momentum. By taking the Weyl identity into Eq. (S2), the vector potential can be expanded into plane waves with different propagation directions:

$$\mathbf{A(r)} = \frac{\omega\mu}{8\pi^2}\mathbf{p}[\iint \frac{1}{k_{za}}e^{i(k_x x + k_y y \pm k_{za} z)}dk_x dk_y],\qquad(S3)$$

where the $\pm$ sign represents the radiative field above/below the dipole. To acquire the electric field distribution for this electric dipole, the following equations are used:

$$\boldsymbol{H}(r) = \frac{1}{\mu}\left[\nabla \times \boldsymbol{A}(r)\right],$$

$$\boldsymbol{E}(r) = -\frac{1}{i\omega\varepsilon}\left[\nabla \times \boldsymbol{H}(r)\right],\qquad(S4)$$

By substituting Eq. (S3) into Eq. (S4) and considering $\nabla \times \rightarrow i\mathbf{k}\times$, the relationship between the electric field and the vector potential of an electric dipole can be expressed as shown in Eq. (S5):

$$\mathbf{E(r)} = \frac{i}{8\pi^2\varepsilon}\frac{1}{k_{za}}[-\mathbf{k^{\pm}}(\mathbf{k^{\pm}}\cdot\mathbf{p}) + k^2\mathbf{p}][\iint e^{i(k_x x + k_y y \pm k_{za} z)}dk_x dk_y],\qquad(S5)$$

where $\boldsymbol{k}^{\pm} = \left(k_x, k_y, \pm k_{za}\right)$ represents the wave vector.

Assuming that the dipole is located at $z = z_0 > 0$, i.e., above the interface between the air and the substrate, the angular spectrum amplitude at $z=0$ is given by:

$$\overset{\circ}{\mathbf{E}}(k_x, k_y; 0) = \frac{i}{8\pi^2\varepsilon}\frac{1}{k_{za}}[-\mathbf{k^{\pm}}(\mathbf{k^{\pm}}\cdot\mathbf{p}) + k^2\mathbf{p}]e^{ik_{za} z_0},\qquad(S6)$$

To enable further discussion of the electromagnetic field propagating into the substrate, it is convenient to introduce the polarization vector basis [9]:

$$\mathbf{e_s} = \frac{\mathbf{e_z} \times \mathbf{k}^{\pm}}{\sqrt{(\mathbf{e_z} \times \mathbf{k}^{\pm}) \cdot (\mathbf{e_z} \times \mathbf{k}^{\pm})}} = \frac{(-k_y, k_x, 0)}{\sqrt{k_x^2 + k_y^2}}, \tag{S7}$$

$$\mathbf{e_p^{\pm}} = \mathbf{e_z} \times \mathbf{k}^{\pm} / k = \frac{\left(\pm k_x k_z, \pm k_y k_z, -(k_x^2 + k_y^2)\right)}{\sqrt{k_x^2 + k_y^2}}, \tag{S8}$$

where the subscripts indicate the s and p polarizations. The electric field can then be expressed as a combination of E_s and E_p:

$$\overset{\circ}{\mathbf{E}}(k_x, k_y; 0) = \frac{ik^2}{8\pi^2 \varepsilon} \frac{1}{k_{za}} \{[\mathbf{e_s} \cdot \mathbf{p}]\mathbf{e_s} + [\mathbf{e_p^{\pm}} \cdot \mathbf{p}]\mathbf{e_p^{\pm}}\} e^{ik_{za}z_0}, \tag{S9}$$

If only the s-component (E_s) is considered, then the electric field can be simplified further as shown in Eq. (S10):

$$\overset{\circ}{\mathbf{E}}_s(k_x, k_y; 0) = \frac{ik^2}{8\pi^2 \varepsilon} \frac{1}{k_{za}} \{\mathbf{e_s} \cdot \mathbf{p}\} e^{ik_{za}z_0}, \tag{S10}$$

It is known that each point in the angular spectrum corresponds to a plane wave with a specific propagation direction, and the electric field transmitting through the interface (the plane at $z = 0$) can be expressed as the field given in Eq. (S10) multiplied by the Fresnel transmission coefficient t_s. The Fresnel coefficient for any multilayer structure or interface can be derived using the transfer matrix method (TMM). [10]

To calculate the far-field electric field distribution inside the substrate, the Weyl identity is used again. Furthermore, the stationary phase method is used and the final far-field electric field can be expressed as Eq. (S11): [6]

$$\begin{aligned} E_s &= \frac{2\pi k_{zg}}{ire^{-ikr}} t_s \overset{\circ}{\mathbf{E}}_s(k_x, k_y; 0) \\ &= \frac{e^{ikr} k^2}{4\pi\varepsilon r} \frac{k_{zg}}{k_{za}} t_s \{\mathbf{e_s} \cdot \mathbf{p}\} e^{ik_{za}z_0}, \\ &= A_0 \frac{k_{zg}}{k_{za}} t_s \frac{[-k_y p_x + k_x p_y]}{\sqrt{k_x^2 + k_y^2}} e^{ik_{za}z_0} \end{aligned} \tag{S11}$$

where A_0 is the scaling factor.

If a row of electric dipoles is arranged along the y-direction, the total electric field of the light

radiating from these dipoles is:

$$E_s^{tot} = \int E_s e^{i\left(-k_y y' + \phi(y')\right)} dy', \tag{S12}$$

where the initial phase of the dipole located at $y = y'$ is $\phi(y')$.

If we assume that the distribution of the initial phase of the Nth dipole is $\phi(y') = k_y' \cdot y'$, then the total field can be simplified as:

$$E_s^{tot} = 2\pi E_s \delta\left(k_y' - k_y\right), \tag{S13}$$

Here, k_y' is the y-component of the incident wave vector (enabled by an externally stimulated field), and y' represents the spatial location of the Nth dipole.

In this case, the far-field electric field may not be zero when the condition $k_y = k_y'$ is satisfied.

Equation (S13) corresponds to the electric field distribution along the white dashed line shown in Fig. 2(b) when $k_y = k_{y0}$. In fact, this field only comes from the scattering that occurs when the wavenumber exceeds k_0; therefore, we simply consider the evanescent components with wavenumbers in the range from k_0 to $1.49k_0$ (where the value of 1.49 is determined by the NA of the collection objective).

The total intensity of the electric fields located on the left (I_L) and right (I_R) sides of the y-axis could be expressed as

$$I_L = A\int_{-k_2}^{-k_1} \left|E_s^{tot}\right|^2 dk_x,$$

$$I_R = A\int_{k_1}^{k_2} \left|E_s^{tot}\right|^2 dk_x, \tag{S14}$$

where $k_1 = \sqrt{k_0^2 - k_y^2}$ and $k_2 = \sqrt{(1.49k_0)^2 - k_y^2}$. We define the parameter I_{L-R} as shown in Eq. (S15) to describe the relationship between I_L and I_R.

$$I_{L-R} = \int_{k_1}^{k_2} \frac{\left|k_x \cdot p_y + k_y \cdot p_x\right|^2}{\left|k_x \cdot p_y - k_y \cdot p_x\right|^2} dk_x, \tag{S15}$$

From the equations above, we can anticipate that two specific cases will appear for these dipoles

10

when arranged in a line. If $k_x \cdot p_y - k_y \cdot p_x = 0$, then I_R will be zero. In this case,

$-k_x \cdot p_y - k_y \cdot p_x = -2k_y \cdot p_x$, and then I_L will be a nonzero value. This case corresponds to unidirectional

radiation (toward the left side of the y-axis) of the dipole array. Similarly, if $-k_x \cdot p_y - k_y \cdot p_x = 0$ and

$k_x \cdot p_y - k_y \cdot p_x = -2k_y \cdot p_x$ are satisfied, then I_R will be nonzero and I_L will be zero. This case

corresponds to unidirectional radiation toward the right side of the y-axis.

The in-plane dipole was defined in Fig. 2(b) in the main text, and its dipole moment can be

expressed as $\boldsymbol{p} = (p_x, p_y) = p_0 (\cos(\varphi_0), \sin(\varphi_0))$. If we take the denary logarithm of I_{L-R}, we can then

obtain the asymmetric curve shown in Fig. 2(c).

The descriptions above clearly verify that asymmetric radiation can be realized by tuning the values

of p_x. and p_y, or by tuning the value of φ_0.

Part 2 Detailed derivation with anisotropic polarization coefficients

In part 1, we only considered the case where the polarization coefficients are equal along the x- and

y-axes. In this part, we discuss the effects of having different polarization coefficients along the x- and

y-axes. The basic relationship between the dipole moment $\boldsymbol{p}$ and the electric field $\boldsymbol{E}$ can be found in

electrodynamics [6]:

$$\boldsymbol{p} = \alpha \boldsymbol{E} , \qquad (S16)$$

In our case, only the in-plane dipole $\boldsymbol{p} = (p_x, p_y)$ is considered, and thus Eq. (S16) can be written

as:

$$\begin{bmatrix} p_x \\ p_y \end{bmatrix} = \begin{bmatrix} \alpha_{xx} & \alpha_{xy} \\ \alpha_{yx} & \alpha_{yy} \end{bmatrix} \begin{bmatrix} E_x \\ E_y \end{bmatrix}, \qquad (S17)$$

Because the cross-polarization coefficients can usually be neglected, equation (S16) can be

simplified as $p_x = \alpha_x E_x$ and $p_y = \alpha_y E_y$ where $\alpha_x = \alpha_{xx}$ and $\alpha_y = \alpha_{yy}$. The directional radiation can then

be obtained if the following equation is satisfied.

$$\frac{p_x}{p_y} = \frac{\alpha_x E_x}{\alpha_y E_y} = \frac{\alpha_x}{\alpha_y} \cdot \frac{a_0}{\tan(\varphi_{max})} = \frac{k_x}{k_y}, \qquad (S18)$$

where $a_0 = E_{x0} / E_{y0}$ (E_{x0}, E_{y0} are the maximum electric amplitude along x- and y- axes). It is easy to

see that α_x / α_y and φ_{max} determine the strong asymmetric radiation from Eq. (S18) with fixed incident amplitude and wavenumbers.

Discussion of optical metrology measurement

In this section, we demonstrate that the strong asymmetric radiation is suitable for measuring the width of subwavelength scatters including nanowires and nanoslits.

As we discuss before, the polarization coefficients ($\alpha_x : \alpha_y$) which are related to the morphology of the subwavelength scattering (including width and height (W, H) of a nanowire when used in the experiments) can influence the asymmetric radiation; therefore, we can derive the value of W by searching φ_{max} when height H is fixed.

With Born approximation and assuming W, $H \ll \lambda$, the polarization coefficients related to geometric size of oval cross section can be written as

$$\alpha_i = V \frac{\varepsilon_r - 1}{1 + L_i (\varepsilon_r - 1)} \quad i=x, \, y, \tag{S19}$$

where ε_r is the relative permittivity of nanowires, $L_x = \left[H / (W + H) \right]$, $L_y = 0$ and $V = \pi^2 WH$.

We assume that the height H is fixed at 55 nm. The results from dipole model can be depicted and compared with that from numerical simulation in Fig. S7a. The inset graph in Fig. S7a shows the simulation model, in which a nanowire with height H and width W is fabricated on the dielectric multilayer. Both curves show the same tendency as the width increased. However, the increasing φ_{max} is slower than β_{max} with increasing width. This is because the Born approximation cannot be satisfied. This will be demonstrated in Fig. S8 though multipole decomposition of total scattering field.

The nanoslit is the complementary structure to the nanowire and is also always used as a coupler for optical surface waves, including SP polaritons (SPPs), BSWs, and evanescent waves[1-5]. For simplicity, only numerical simulations were performed to verify the proposed metrology method. The inset graph in Fig. S7b shows the simulation model, in which a nanoslit with depth D and width W is etched on the dielectric multilayer. In the simulation, the depth is fixed at 10 nm. The simulated curve shows that β_{max} decreases gradually with increasing nanoslit width. This trend is opposite to that shown in Fig. 4c and S7a, because the nanoslit inside the multilayer structure represents the inverse structure to that of a nanowire on the multilayer structure. The simulated curve clearly verifies that the nanoslit width can also be derived from the β_{max} value. The curves in Fig. S7 demonstrate that the proposed method is also applicable to nanowires with various cross-sectional shapes including oval cross-section
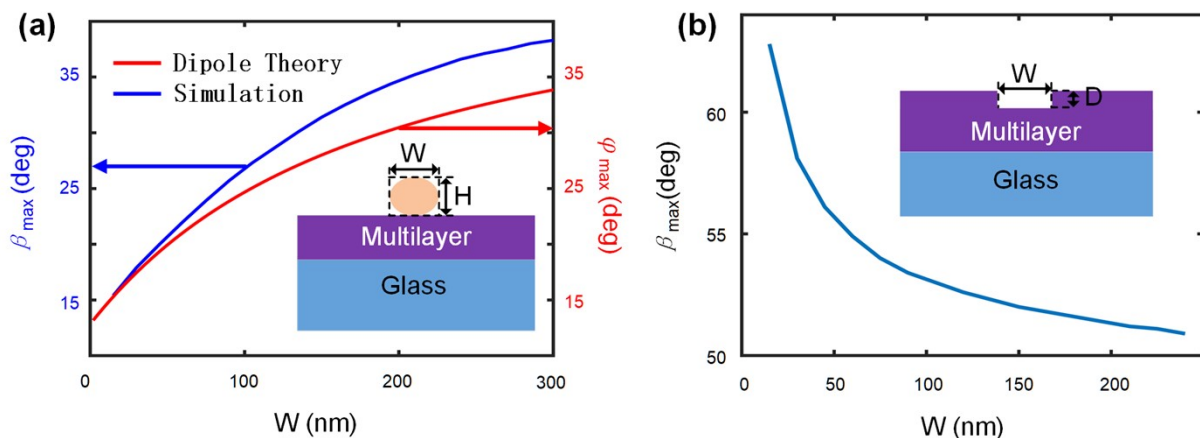
12

nanowires and nanoslits.

Figure S7. Deriving the width of (a) oval cross-section nanowires and (b)nanoslits.
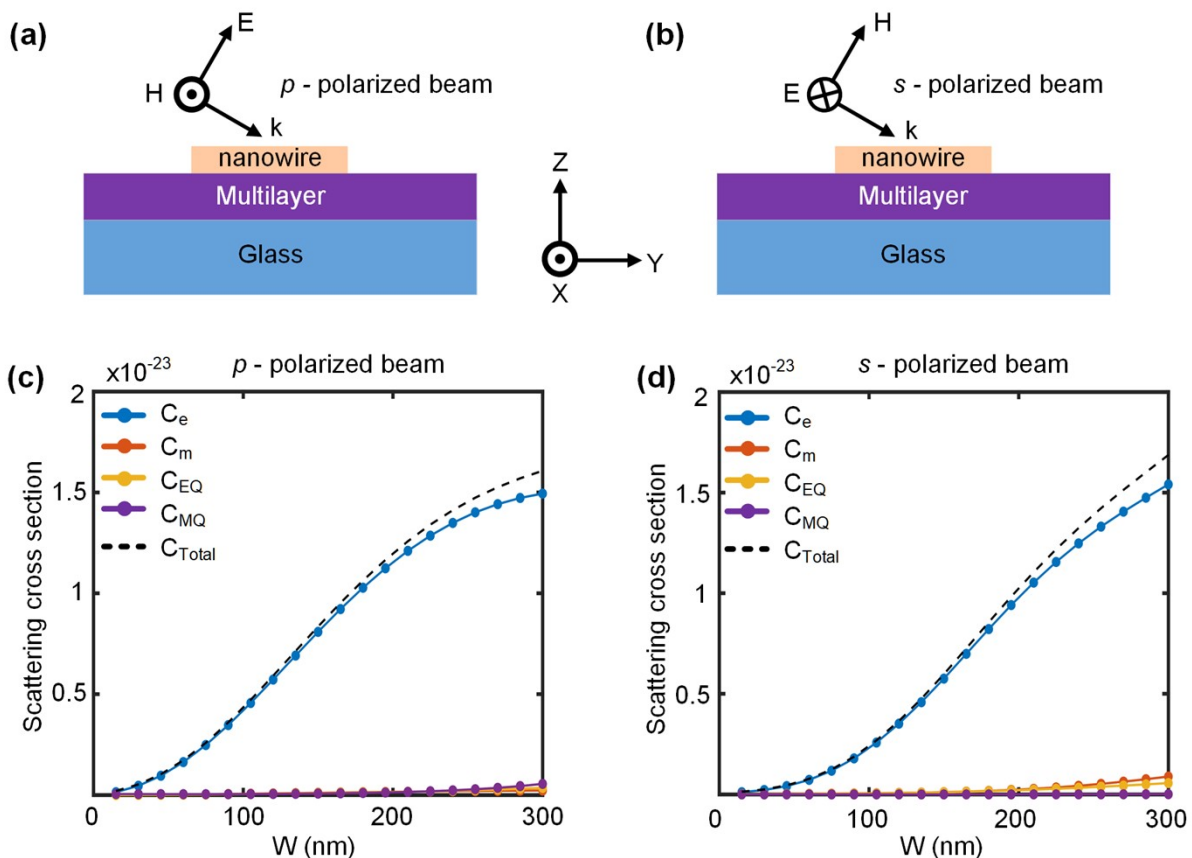

Figure S8. Decomposition of the total scattering field into multipole contributions. (a), (b) Schematics of the model of numerical simulation (FDTD). Nanowire is illuminated by *p*-polarized and *s*-polarized beams, respectively. (c, d) The corresponding calculated total scattering cross-section (C_{total}), and the scattering cross-sections from an electric dipole (C_e), a magnetic dipole (C_m), an electric quadrupole (C_{EQ}), and a magnetic quadrupole (C_{MQ}).

13

Measurement of height

In our work, a row of electric dipoles is realized with a single nanowire under tilted illumination from a plane wave. The height of a nanowire (H) can be derived from Eq. (S20), as described in Ref XXX[8, 11]. To distinguish the scattering field and transmitted incident light, the in-plane wavenumbers propagating field ranges from $0.95k_0$ to k_0. Figure S9 presents the relationship between R and geometric size of nanowires. The intensity values were derived from the simulated BFP images. The heights range from 20 nm (H20) to 80 nm (H80) with fixed internal 10 nm. This intensity ratio decreases with increasing height (H). This intensity ratio remains nearly the same for nanowires with a fixed H and various width (W) values. These phenomena mean that this ratio is sensitive to the nanowire height, but it is not sensitive to the nanowire width. Therefore, the nanowire's height can be derived from this ratio.

$$R = \frac{\int_{k_1}^{k_2} |E_s|^2 \, dk_x}{\int_{k_3}^{k_1} |E_s|^2 \, dk_x}, \qquad (S20)$$
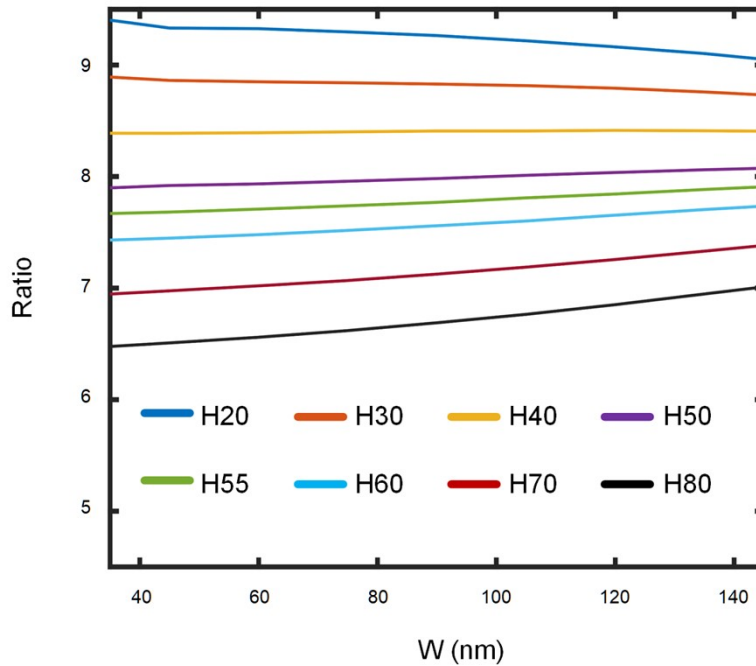

Figure S9. Calculated curves of intensity ratio *vs.* nanowire width.
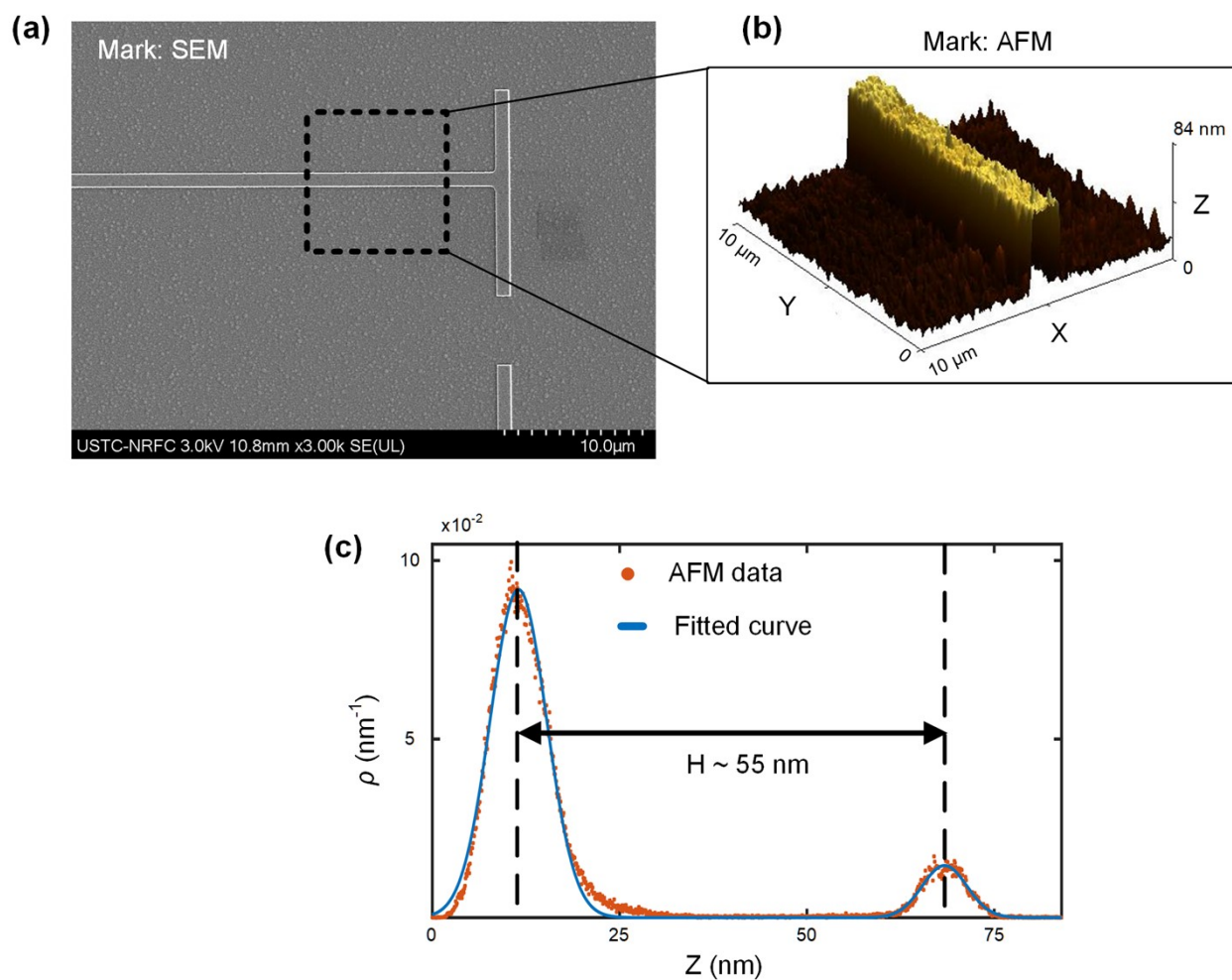
14

Figure S10. Height measurement with AFM. (a) SEM and (b) AFM images of the mark. (c) Distribution of the probability density of z (nm) obtained from the AFM image in (b), which gives the average height of the nanowire (approximately 55 nm).

Reference:

1. López-Tejeira, F.; Rodrigo, S. G.; Martín-Moreno, L.; García-Vidal, F. J.; Devaux, E.; Ebbesen, T. W.; Krenn, J. R.; Radko, I. P.; Bozhevolnyi, S. I.; González, M. U.; Weeber, J. C.; Dereux, A., Efficient unidirectional nanoslit couplers for surface plasmons. *Nature Physics* **2007,** *3* (5), 324-328.

2. Lee, S.-Y.; Lee, I.-M.; Park, J.; Oh, S.; Lee, W.; Kim, K.-Y.; Lee, B., Role of Magnetic Induction Currents in Nanoslit Excitation of Surface Plasmon Polaritons. *Physical Review Letters* **2012,** *108* (21), 213907.

3. Rodríguez-Fortuño, F. J.; Marino, G.; Ginzburg, P.; O'Connor, D.; Martínez, A.; Wurtz, G. A.; Zayats, A. V., Near-Field Interference for the Unidirectional Excitation of Electromagnetic Guided Modes. *Science* **2013,** *340* (6130), 328-330.

4. Lefier, Y.; Grosjean, T., Unidirectional sub-diffraction waveguiding based on optical spin-orbit coupling in subwavelength plasmonic waveguides. *Opt. Lett.* **2015,** *40* (12), 2890-3.

5. Qin, Y.; Ji, B.; Song, X.; Lin, J., Ultrafast spatiotemporal control of directional launching of surface plasmon polaritons in a plasmonic nano coupler. *Photonics Research* **2021,** *9* (4).

6. Novotny, L.; Hecht, B., *Principles of nano-optics*. Cambridge university press: 2012.

7. Mueller, J. P. B.; Capasso, F., Asymmetric surface plasmon polariton emission by a dipole emitter near a metal surface. *Physical Review B* **2013,** *88* (12).

8. Xi, Z.; Urbach, H. P., Retrieving the Size of Deep-Subwavelength Objects via Tunable Optical Spin-Orbit Coupling. *Phys Rev Lett* **2018,** *120* (25), 253901.

9. Vázquez-Lozano, J. E.; Martínez, A.; Rodríguez-Fortuño, F. J., Near-Field Directionality Beyond the Dipole Approximation: Electric Quadrupole and Higher-Order Multipole Angular Spectra. *Physical Review Applied* **2019,** *12* (2).

10. Yeh, P.; Yariv, A.; Hong, C.-S., Electromagnetic propagation in periodic stratified media. I. General theory*. *J. Opt. Soc. Am.* **1977,** *67* (4), 423-438.

11. Dasgupta, A.; Deschamps, J.; Matti, U.; Hubner, U.; Becker, J.; Strauss, S.; Jungmann, R.; Heintzmann, R.; Ries, J., Direct supercritical angle localization microscopy for nanometer 3D superresolution. *Nat Commun* **2021,** *12* (1), 1180.